Article

Carbene-Metal-Amide Polycrystalline Materials Feature Blueshifted Energy yet Unchanged Kinetics of Emission

Jiale Feng, Elliot J. Taffet, Antti-Pekka M. Reponen, Alexander S. Romanov, Yoann Olivier, Vincent Lemaur, Lupeng Yang, Mikko Linnolahti, Manfred Bochmann, David Beljonne, and Dan Credgington

Just Accepted

Carbene-Metal-Amide Polycrystalline Materials Feature Blueshifted Energy yet Unchanged Kinetics of Emission

Jiale Feng[1†], Elliot J. Taffet[2†], Antti-Pekka M. Reponen[1], Alexander S. Romanov[3], Yoann Olivier[5], Vincent Lemaur[4], Lupeng Yang[1], Mikko Linnolahti[6], Manfred Bochmann[3], David Beljonne[4]*, Dan Credgington[1]*

[1]Cavendish Laboratory, Department of Physics, University of Cambridge, JJ Thomson Avenue, Cambridge CB3 0HE, United Kingdom.

[2]Department of Chemistry, Stanford University, Stanford, California 94305, United States.

[3]School of Chemistry, University of East Anglia, Earlham Road, Norwich NR4 7TJ, United Kingdom.

[4]Laboratory for Chemistry of Novel Materials, University of Mons, Place du Parc 20, 7000 Mons, Belgium

[5]Unité de Chimie Physique Théorique et Structurale & Laboratoire de Physique du Solide, Namur Institute of Structured Matter, Université de Namur, Rue de Bruxelles, 61, 5000 Namur, Belgium.

[6]Department of Chemistry, University of Eastern Finland, Joensuu Campus, FI-80101 Joensuu, Finland

ABSTRACT: The nature of carbene-metal-amide (CMA) photoluminescence in the solid state is explored through spectroscopic and quantum-chemical investigations on a representative Au-centred molecule. The crystalline phase offers well-defined coplanar geometries—enabling the link between molecular conformations and photophysical properties to be unravelled. We show that a combination of restricted torsional distortion and molecular electronic polarisation blueshift the charge-transfer emission by around 400 meV in the crystalline versus the amorphous phase, through energetically raising the less-dipolar S_1 state relative to S_0. This blueshift brings the lowest charge-transfer states very close to the localised carbazole triplet state, whose structured emission is observable at low temperature in the polycrystalline phase. Moreover, we discover that the rate of intersystem crossing and emission kinetics are unaffected by the extent of torsional distortion. We conclude that more coplanar triplet equilibrium conformations control the photophysics of CMAs.

1. INTRODUCTION

Carbene-metal-amides (CMA) are a large family of organometallic donor-bridge-acceptor photoemitters that are promising candidates for thin-film light-emitting diodes. [1–6] CMA1, as the archetype of this group of molecules, employs cyclic (alkyl)(amino)carbene (CAAC) acceptor and carbazole (Cz) donor bridged by a gold (Au) atom, showing high photoluminescence quantum efficiency (80-90%) in solid films from states involving electron transfer from donor to acceptor, good chemical stability and fast intersystem crossing. [1–6] The σ-donating nature of the carbene ligand leads to a large permanent electrostatic dipole moment in the ground state. Photoluminescence mainly occurs via the triplet charge-transfer (CT) state and is thermally activated, with characteristic activation energy around 70-80 meV and sub-microsecond characteristic emission lifetime in both solution-processed and sublimed devices at 300 K.[2,7]

CMA1, in common with many CMA materials, exhibits an energetic minimum in the ground state with donor and acceptor ligands approximately coplanar, while the excited singlet minimum of the isolated molecule occurs when donor and acceptor ligands are approximately orthogonal[2,8–11], indicative of twisted-intramolecular-charge-transfer (TICT) character. A range of emission energies and conformations are therefore accessible between the ground-state and excited-state minima, because in the solid state the molecules encounter different steric and dielectric environments. Significant differences in the photophysics are hence expected when varying the environment of the molecules, as increasing torsion angle leads to reductions in oscillator strength, exchange energy and molecular symmetry.[12–14] The search for next-generation electroluminescent materials requires that we understand the

impact of these changes, in order to design materials with "ideal" photophysical characteristics. Such material design is predicated on resolving the interplay between emitter conformation and environmental embedding, which is the issue motivating this investigation.

Multiple models now exist for how torsional motion impacts triplet emission in TADF materials in general, and CMAs in particular. Föller and Marian suggested that coupling between S_1 and T_1 is dependent on molecular geometry, and at 300K is spin-vibronic in nature, while low-temperature phosphorescence involves direct spin-orbit coupling via an S_2 state.[9] Further calculations by Penfold et al. concluded that indirect SOC (i.e. $S_1 - T_n - T_1$) assisted by torsional motion impacts the rate of triplet harvesting.[11] Taffet et al. found from multireference orbital-optimisation calculations that despite the fact that torsional motion is able to narrow the CT $S_1 - T_1$ energy gap, a concomitant decrease in oscillator strength and spin-orbit coupling occurs. They concluded that the distortion of the carbene carbon-metal-amide nitrogen central axis followed by carbene carbon-nitrogen bond stretching facilitates intersystem crossing (ISC).[15] Current models of thermally-activated emission in organic materials suggest that orthogonal D-A groups are a necessary requirement for CT emission, and experimental evidence exists that restriction of torsional motion leads to a degradation in performance.[14,16]

Here we realise an experimental method to achieve polycrystalline thin films of CMA materials, allowing the link between geometry and photophysics to be probed directly by experiment. We find that torsional restriction together with molecular polarisation significantly blueshift the photoluminescence. In spite of this emission-energy blueshift, emission kinetics remain constant across material phases—a phenomenon we ascribe to the partially twisted nature of the triplet geometric optimum that remains accessible under conditions of frustrated nuclear reorganisation. On the other hand, the singlet potential is modified significantly by crystallisation, such that its energetic minimum lies proximal to that of the nearly coplanar triplet. Thus, crystallisation pushes the density of emissive states closer to that of phosphorescent, carbazole-based, triplets. The photophysical behaviour, in turn, is largely unchanged in the solid state—dominated by the kinetics of spin crossover at more coplanar conformations associated with the relaxed triplet.

Consequently, we find a constant activation energy for delayed luminescence. We interpret this as corresponding to the exchange energy at a partially twisted triplet geometry. Thus, while the absolute value of emission energy is dependent on the environment, the *relative* energy between the lowest-lying singlet and triplet states—the exchange splitting—is determined by molecular conformation, and it is this splitting which primarily influences radiative triplet decay. Experimental spectroscopy and quantum chemistry are reconciled under the physical picture that constrained torsional distortion leads to a singlet minimum-energy conformation resembling that of the triplet, which appears unperturbed by the solid-state environment.

2. RESULTS AND DISCUSSION

2.1. THIN-FILM CRYSTALLISATION

Although single crystals and crystalline powders offer well-defined geometries, they are typically optically thick and difficult to assess using thin-film characterisation techniques and unsuitable for incorporation into devices and device-like thin films. We therefore first describe a method to produce thin films of crystallised CMA1 hosted in a plasticising poly(ethyleneoxide) (PEO) matrix. PEO is a polar matrix with averaged dipole moment per constitutional repeating unit of around 1D at 25 °C.[17] A range of PEO variants with weight-average molecular weight (M_w) from 2,000 to 8,000,000 Da were explored. The glass transition temperatures for PEO in this range of polymerisation are all below 0 °C, allowing it to act a thin-film plasticiser at ambient temperature.[18] For the structural and photophysical characterisation detailed below, we employed PEO with Mw of 100,000 Da since spin-cast films offer appropriate optical density (O.D.) for photophysical characterisations. Qualitatively similar results were obtained for all Mw in this range. CMA1 was mixed at 80 wt.% in PEO in chlorobenzene solution. Spin coating at 1,200 rpm for 40 seconds on fused quartz substrates (Spectrosil) resulted in thin films exhibiting green photoluminescence. Upon annealing on a hotplate at 120 °C for 1 min, photoluminescence progressively shifts to blue, with conversion to the blue-emitting phase essentially complete after 20 seconds at 120 °C, see **Video S 1**. No regions of residual green emission are observed.

Figure 1 a presents the XRD pattern of as-cast and annealed CMA1 thin films. As-cast samples exhibit little diffraction signal, and we consider these to comprise largely amorphous material. After annealing, samples show strong diffraction peaks at 8.2, 8.7 and 10.3 degrees which match with diffraction peaks assigned to the (002), (100) and (101) planes in polycrystalline powder samples.[2] The crystalline phase corresponds to a largely coplanar geometry close to the ground-state minimum (torsion angle of 20°) with alternating head-to-tail alignment of CMA molecules. The PEO matrix also shows partial crystallisation after annealing, with two peaks at 19.2 and 23.4 degrees as reported in literature and assigned to the (120) planes and overlapping reflections from the (032), ($\bar{1}$32), (112), ($\bar{2}$12), ($\bar{1}$24), ($\bar{2}$04), and (004) planes.[19–22] We thus consider that the soft, polar, PEO environment enables nucleation and growth of CMA crystals to create a thin film of polycrystalline CMA1 embedded in an optically inert PEO matrix. Crystallisation can also be induced in other matrices under harsher experimental conditions and/or over longer times, as detailed in **Table S 1**. We will henceforth refer only to CMA1 crystallised within a PEO matrix.

Non-resonant Raman spectra of as-cast and annealed CMA1:PEO samples are shown in **Figure 1 b**. Since the molecular species are identical, spectral differences represent changes in vibrational freedom within different forms. Low-frequency rotation between donor and acceptor is revealed at low Raman shift peaks (< 200 cm^{-1}), which sharpen significantly in the crystalline phase. We interpret this as a decrease in conformational disorder associated with crystallisation. Just as important as the conformational restriction is the dynamic polarisation conferred by the induced dipoles of surrounding CMA1 molecules in the solid state. The unique environment conferred by crystallisation manifests in Raman intensity reduction of the carbene-nitrogen bond-stretching mode ($\sim$1500 cm^{-1}), complemented by enhancement of the carbene bending modes at $\sim$1000 and $\sim$1300 cm^{-1}. As such, the environment non-trivially influences the molecular polarisability tensor, meaning that considerations of molecular

relaxation must be coupled with considerations of the surrounding environment.
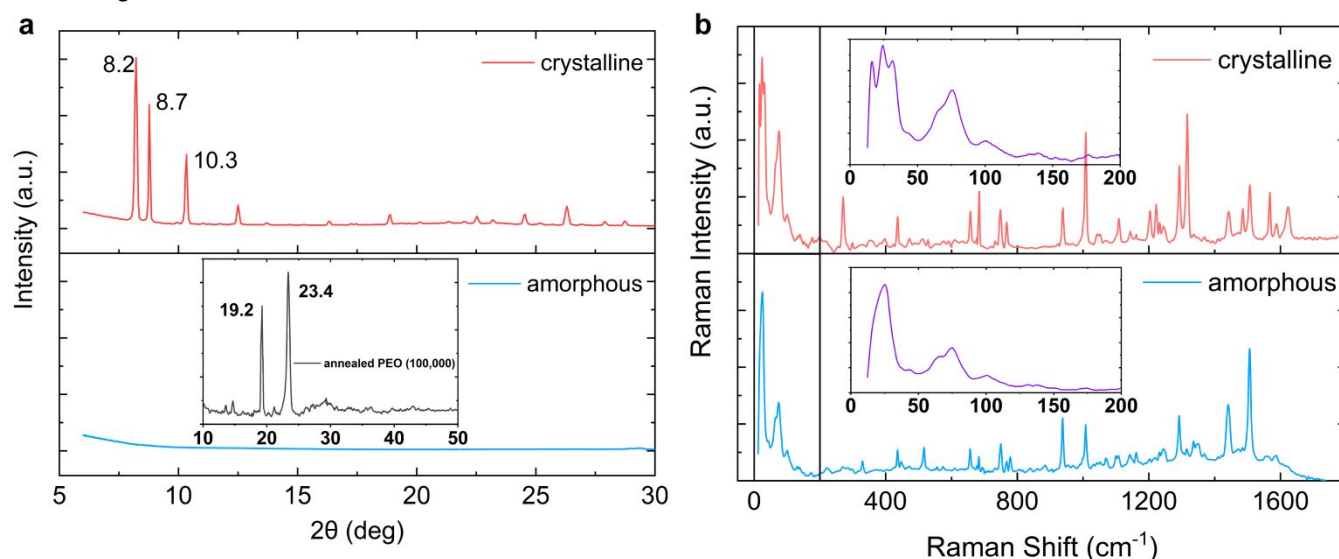

Figure 1: a X-ray diffraction of crystalline and amorphous CMA1. Three distinct peaks appear at 8.2, 8.7 and 10.3 degrees. The inset shows weak crystallisation of annealed PEO (100,000) with two peaks at 19.2 and 23.4 degrees. b Raman spectra of crystalline and amorphous CMA1. Raman shift below 200 cm^{-1} is magnified. Films were drop cast from CMA1 chlorobenzene solution (20 mg/ml) mixing with 20 wt.% PEO (Mw 100,000 Da) in a nitrogen glovebox, followed by annealing at 120 ˚C for 1 min to crystallise.

2.2. STEADY-STATE SPECTROSCOPY

Figure 2 a presents the steady-state absorption and photoluminescence (PL) spectra of amorphous and crystallised CMA1 thin films, and CMA1 in toluene solution. The broad absorption peak at around 390 nm for films and 405 nm for solution represents direct excitation to the singlet charge-transfer (CT) state while higher-energy peaks are associated with CAAC/Cz locally excited (LE) states and their vibronic progressions: 370 nm (short-axis-polarised Cz transition), 305 nm (long-axis-polarised Cz transition), and 270 nm (transitions from both CAAC acceptor and Cz donor).

In the crystalline phase, the oscillator strength of intraligand transitions at 305 nm and 270 nm are highly suppressed. This is consistent with the short-axis-polarised Cz singlet 370-nm transition inheriting oscillator strength from the linear on-axis anti-alignment of CMA1 dipoles in this phase. In addition, the CT absorption feature narrows, consistent with a reduction in both conformational and electrostatic disorder leading to a narrower density of states (DoS). The photoluminescence peak of CMA1 in toluene solution is around 525 nm, in amorphous film around 520 nm, and in crystallised film 450 nm. The crystalline phase therefore exhibits a substantial blueshift of 400 meV relative to the toluene solution and 370 meV relative to the amorphous film. This blueshifted emission in the crystalline phase was also observed in other organic emitters.[23] The Stokes shift, measured from CT absorption to CT emission, which represents twice the reorganisation energy induced by conformational relaxation from S_1 to S_0 in a harmonic picture of potential energy surfaces, decreases from 0.7 eV in solution to 0.44 eV in crystal. This implies smaller structural changes in the crystal during the excited-state relaxation process. The emission spectrum of crystalline material shows negligible contribution from the green-emitting amorphous phase. The photoluminescence quantum efficiency of crystallised thin film was measured to be 55%.

2.3. TIME-RESOLVED SPECTROSCOPY

Figure 2 b shows the room temperature time-resolved photoluminescence peak energy and integrated emission with time. The energy offset between the amorphous and crystalline CMA1 is large, around 350 meV before 4 μs, beyond which PL of the crystalline sample rapidly redshifts to an amorphous-like emission energy. We interpret this as a small contribution to emission from remnant non-crystalline CMA1 that might be initially photoexcited, leading to a long-lived tail in cumulative counts after 4 μs. The long lifetime of this emission implies that molecular conformations exist in the amorphous sample that are detrimental to rapid triplet harvesting—and that these are absent in the purely crystalline phase.

Figure 2 c presents the normalised emission kinetics. By monoexponential fitting to the blue region (5 ns – 4000 ns) in emission kinetics, a luminescence lifetime of 1.05 μs is yielded for crystalline CMA1 at room temperature, and 0.79 μs for the amorphous phase. By comparison, emission kinetics in deoxygenated toluene solution are monoexponential with lifetime 1.1 μs. Energy relaxation to a quasi-equilibrium within the DoS is observed for solid samples, with the degree of relaxation smaller for crystalline CMA1 (around 93 meV compared to 136 meV in amorphous films, see **Figure 2 b**). This indicates a narrower DoS for crystalline films, consistent with absorption and Raman spectroscopy. A broad excited-state DoS may originate from both variations in molecular conformation, and from the relative polarisation of the environment around individual chromophores, which varies with their separation and relative orientation.[24] In amorphous films, these parameters are randomly distributed, resulting in a Gaussian distribution of polarisation-induced energy shifts.
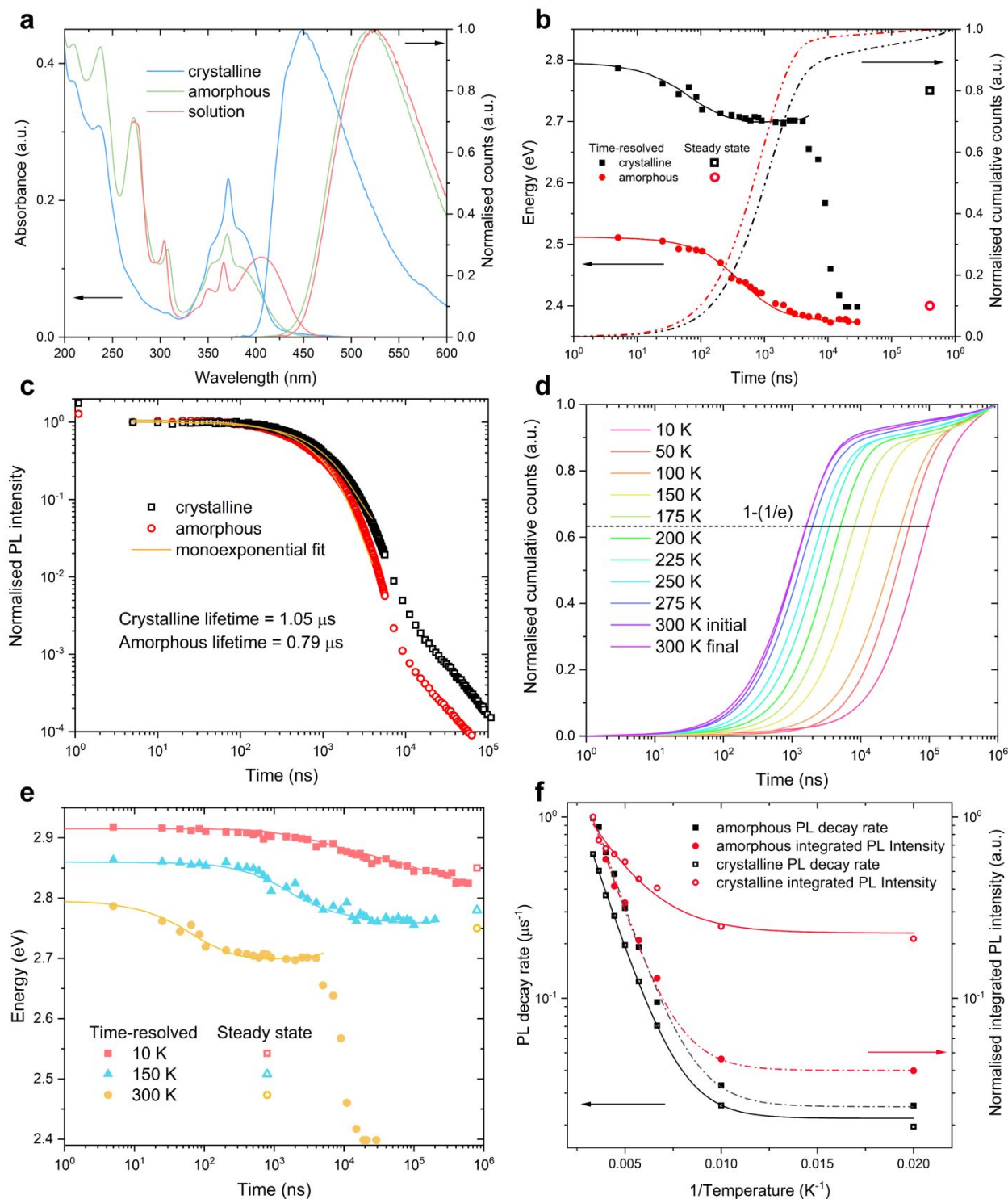
Figure 2: a Steady-state absorption and normalised photoluminescence spectra of CMA1 in toluene solution (1 mg/ml), amorphous and crystalline CMA1 thin films. b Room temperature time-resolved photoluminescence peak energy of amorphous and crystalline CMA1 to track the spectral diffusion. Solid lines are results of Monte-Carlo simulation. Dotted lines are room temperature emission integral. c Normalised delayed emission kinetics with monoexponential fits to crystalline and amorphous CMA1 within the 5 – 4000 ns time range. Lifetimes of 1.05 μs and 0.79 μs are yielded respectively for the crystalline and amorphous phases. d Cryogenic emission integral of crystalline CMA1 at a temperature series with 1-(1/e) labelled as the characteristic luminescence lifetime. "Initial" data taken at 300 K before cooling the film to 10 K, "Final" data upon warming back to 300 K after low-temperature measurements. e Cryogenic time-resolved PL peak position of crystalline CMA1 at 10 K, 150 K, and 300 K. Lines are results of Monte-Carlo simulation. f PL decay rate and integrated PL intensity of crystalline and amorphous CMA1 at different temperatures as a function of 1/Temperature. PL decay rate is the reciprocal of characteristic luminescence lifetime from the cryogenic emission integral. Fitting an Arrhenius-type model $\left(y = A e^{\left(-\frac{E_A}{k_B T} \right)} \right)$ to the data (lines)

yields activation energies: E_Ak (crystalline) = 65 meV, E_APL (crystalline) = 42 meV, E_Ak (amorphous) = 69 meV, E_APL (amorphous) = 68 meV.

At low temperature, characteristic luminescence lifetimes (taken for cumulative emission to reach 63% (1-(1/e)) of the total) increase by approximately a factor of 50 for both crystalline and amorphous CMA1, from 1.6 µs to 94.2 µs for crystalline and 0.97 µs to 60.2 µs for amorphous samples at 10 K, see **Figure 2 d** and **S 1**. The activation energies extracted from an Arrhenius fit to PL decay rate of both samples are similar, 65 meV and 69 meV, as shown in **Figure 2 f**. This value

agrees nicely with the computed exchange splitting of 71 meV at the CMA1 triplet optimized geometry from state-averaged multireference orbital optimisation (Supporting Information). Note that the characteristic activation energies inferred from the integrated PL intensity show a lower value for the crystallised sample of 42 meV compared to 68 meV for the amorphous sample, indicating an interplay between thermally activated radiative and nonradiative decay rates for the crystalline sample.
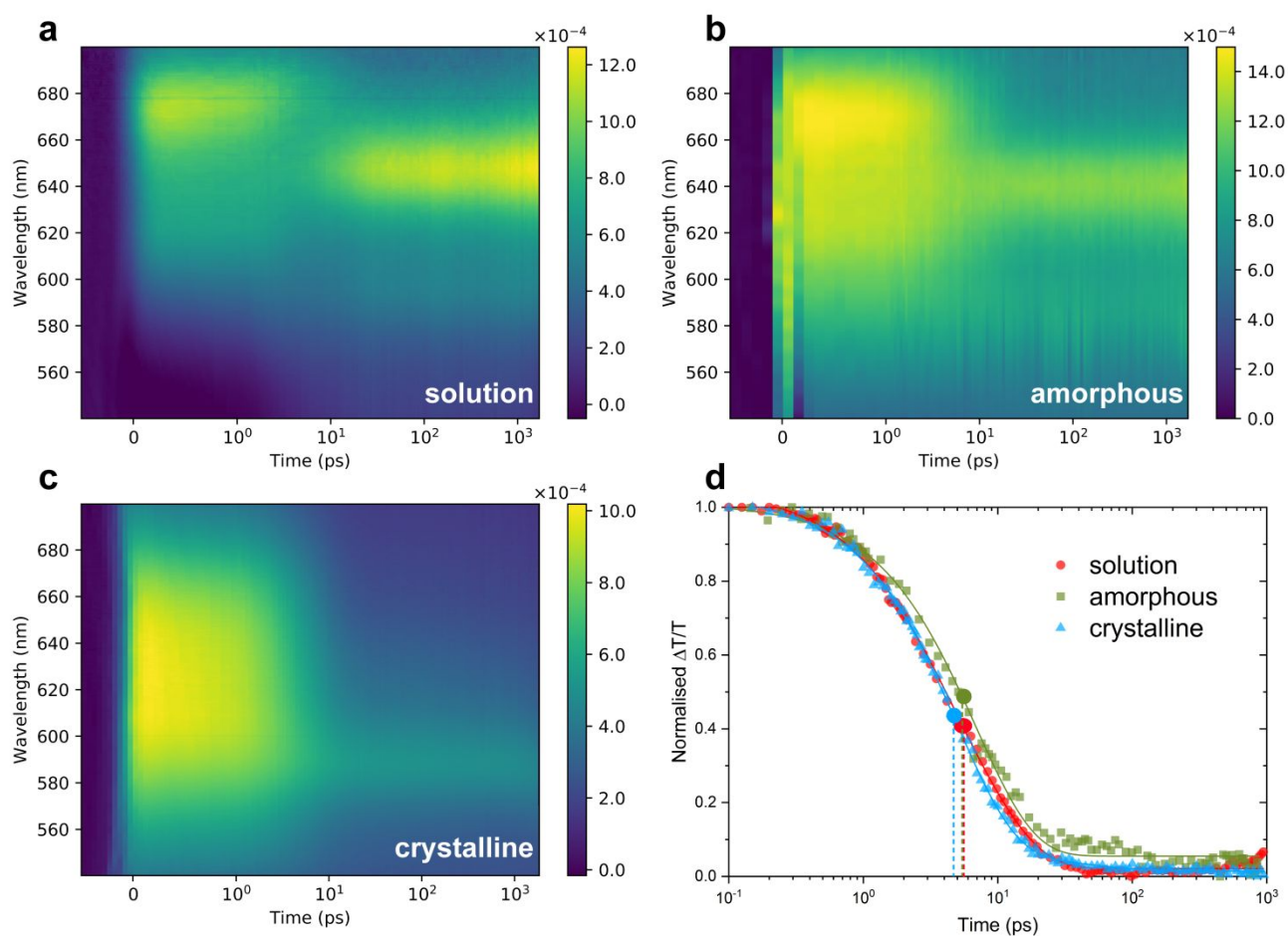

Figure 3. Room temperature transient absorption spectra of a CMA1 in toluene at 1 mg/ml, b neat amorphous CMA1 film, and c crystalline CMA1 film on picosecond-nanosecond time scales. The intensity is shown in $\Delta T/T$, the fractional change in transmission. Samples were pumped at 400 nm under 120 µW pump power for films and 100 µW for solution. d presents the normalised deconvoluted singlet kinetics of solution, amorphous and crystalline phases. The intersystem crossing time of each sample is estimated by the crossover of singlet and triplet kinetics labelled by spots, around 5 ps for all samples. Solid lines are a guide to the eye. The triplet growth kinetic is not included for clarity. Full kinetics are shown in **Figure S 6**. Spectral deconvolution is achieved by isolating co-varying regions of the TA spectra by iterative application of a genetic algorithm. The full details of this approach is described in reference.[25,26] Singular value decomposition of the TA maps reveal two dominant components. As such, the genetic algorithm was restricted to find two independent time-varying species.

PL from the CT state blueshifts with decreasing temperature, consistent with a narrowing of the thermally broadened DoS toward coplanar conformers, a reduction in electrostatic disorder due to thermal motion, and arrested spectral relaxation, see **Figure 2 e.** Below 150 K, the blueshift of the CT state in crystalline material uncovers structured emission, which we

assign to phosphorescence from triplets localised to the carbazole ligand, see **Figure S 3**. By comparison to structured phosphorescence observed in frozen MeTHF (**Figure S 4**), we estimate the localised carbazole triplet energy to be approximately 2.95 eV above the ground state. By contrast, in amorphous CMA1, the carbazole triplet cannot be accessed from the relaxed CT state, and no structured emission is observed even at low temperature. The presence of parasitic

emission from the localised carbazole triplet precludes direct comparison of CT phosphorescence rates between crystalline and amorphous samples.

Turning to triplet dynamics, the spectral migration shown in **Figure 2 b and e** is modelled by considering a Monte-Carlo simulation of 3D triplet diffusion through a Gaussian density of states, as described by Movaghar et al.[27] To reproduce the trends observed, the width of the amorphous-phase DoS (48 meV) is found to be larger than for the crystalline phase (30 meV), as expected. A Marcus-type activated hopping probability (**Eq. S3**) is required to reproduce the observed temperature dependence, and yields a lower characteristic reorganisation energy (λ) of 140 meV for transport in the crystalline phase, corresponding to an activation energy of $E_a = \lambda/4 = 35$ meV, compared to 240/60 meV in the amorphous phase.

Figure 3 a, b, and **c** present the transient absorption (TA) spectra of CMA1 in toluene (1 mg/ml), neat amorphous CMA1 film, and crystalline CMA1 picosecond-nanosecond time scales. Consistent with previous analyses, we assign the early-time photo-induced absorption (PIA) feature to photogenerated singlets, and the later-time PIA feature to triplets formed following intersystem crossing.[2] In solution, the edge of a stimulated emission can also be observed, which shares kinetics with the singlet. The energy and oscillator strength of PIAs in this spectral range vary in each phase. **Figure 3 d** and **Figure S 6** show the normalised deconvoluted singlet and triplet kinetics in each phase. The intersystem crossing (ISC) time of each sample is estimated from the crossover of singlet and triplet kinetics and is found to be identical, within experimental error, at around 5 ps in all phases.

2.4. COMPUTATIONAL SIMULATIONS

To understand these results, we turn to quantum-chemical simulations of the CMA1 crystal environment. The crystal environment constitutes long-range order with intermolecular packing representative of a thermodynamic minimum-energy configuration of ground-state molecules, which can be approximated as a cluster of molecules with relative orientation determined by the crystal structure. We therefore consider a cluster with an embedded CMA1 molecule flanked on either side of a one-dimensional array by anti-aligned CMA1 dipoles and packed in other dimensions by neighbouring molecules in the cell as shown in **Figure 4**. Incorporating this environment of molecules leads to physical hindrance of intramolecular torsion (a classical effect) and electronic polarisation of the excitations (a quantum effect) in the embedded CMA1 molecule, combining to blueshift the S_1-S_0 transition energy, as described below.

2.4.1 CONFORMATIONAL FRUSTRATION IN THE CRYSTAL

We analyse the results of S_1-state geometry optimisation performed either in the vacuum phase or in the crystalline environment. In the latter case, we apply an embedding

Quantum-Mechanics/Molecular-Mechanics (QM/MM) scheme to account for possible frustration effects in the solid (see Methods for details). As a matter of fact, the geometry optimisations alone suggest that photoluminescence blueshifting may be due in part to hampered nuclear reorganisation—restricted intramolecular torsion caused by the steric hindrance within the CMA1 crystalline cluster. While full rotation to an orthogonal torsional angle is predicted for a single-molecule S_1 state optimisation in the gas phase, a retention of effective coplanarity (around 20° torsional angle) is instead obtained for the S_1 geometry of CMA1 in its simulated cluster environment. Frustrated torsion manifests as a stagnation of the S_1-T_1 energy gap following bond stretching within the initial optimisation steps leading to the converged geometry. Thus, the energetic stabilisation initially appears equivalent in the crystal and vacuum phases before diverging upon activation of torsional modes in the vacuum, which relaxes the S_1 (^{1}CT) state to the point of effective degeneracy with the T_1 (^{3}CT) state. This is in contrast to the finite, albeit small, S_1-T_1 energy gap retained throughout crystal-phase S_1 optimisation. Moreover, the oscillator strength remains non-negligible in the minimum-energy conformation of the crystal S_1 state. In contrast, the oscillator strength is diminished to essentially zero following torsion in the vacuum optimisation. Ultimately, the (simulated) loss of additional reorganisation energy from the suppressed torsional degrees of freedom raises the S_1 energy relative to that of S_0/T_1 at an emissive geometry featuring enhanced S_1-S_0 oscillator strength.

2.4.2 ELECTRONIC POLARISATION IN THE CRYSTAL

Due to a more pronounced dipole moment in the ground-state electronic configuration, the polarisation energy from the surrounding CMA1 environment also leads to blueshifted emission. We measure polarisation energy in molecular clusters extracted from the crystalline phase but now adopting a full quantum-chemical model, combining the Tamm-Dancoff-Approximate Time-Dependent Density Functional Theoretical (TDA-DFT) framework with a long-range asymptotically correct LC-ω-PBE tuned DFT functional (see Methods)[28–30]. It is indeed critical to include the dynamic (electronic) polarisation response of the 'solute' to the varying ground- or excited-state charge distribution of the surrounding 'solvent' and this requires either a polarisable classical force-field or a full quantum treatment, which is preferred here. The TDA-DFT/LC-ω-PBE results in **Table 1** agree with experiment on two major fronts. First, the emission-energy result in the vacuum phase (1.92 eV, 646 nm) bounds the experimental dilute-solution emission energy from below—understandable in light of the destabilising effect a polarisable solvent has on emission relative to having no polarisable environment at all. Second, the computed blueshift in the crystal emission energy (2.84 eV, 436 nm) of 0.92 eV positions the crystal emission spectrum within the blue colour range as observed experimentally.
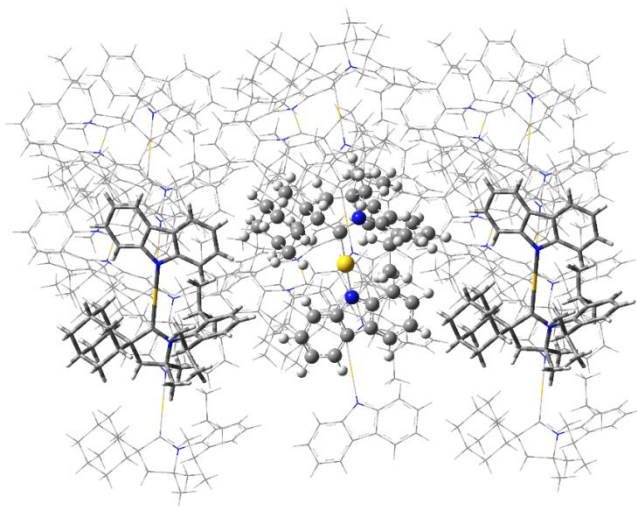
Figure 4. Illustration of a molecular cluster used to simulate the crystal environment where an embedded CMA1 molecule is flanked on either side of a one-dimensional array by anti-aligned CMA1 dipoles and packed in other dimensions by neighbouring molecules in the cell.

Table 1. Emission Energy (ΔE) and Colour in the Simulated Crystal Phase Compared to Vacuum at the TDA(LC-ω-PBE/def2-SVP) level of theory.

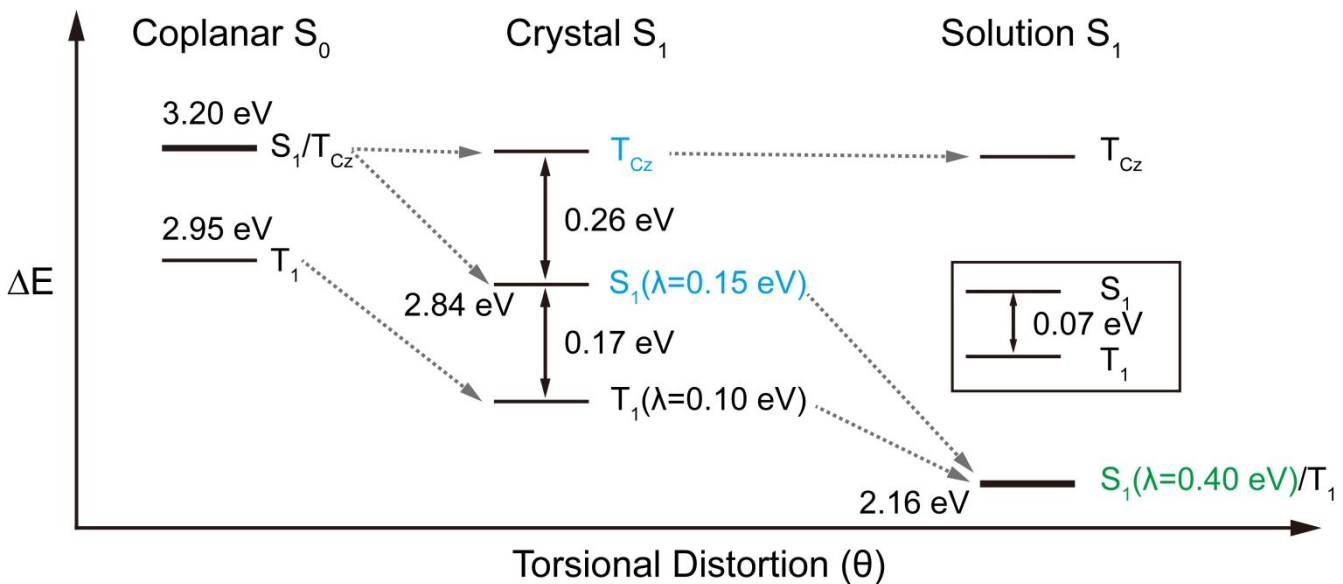| System/Geometry	ΔE (eV)	ΔE (nm)	Emission colour
Crystal/S_1	2.84	436	Dark blue
Vacuum/S_1	1.92	646	Reddish orange

Figure 5. Summary of CMA1 phase-dependent photophysics. At the coplanar S_0 geometry (identical for solution and solid phases), S_1 and T_{Cz} are quasidegenerate, while at the solution S_1 geometry (featuring complete torsional distortion), S_1 and T_1 are quasidegenerate. While the 0.4-eV reorganisation energy of S_1 in solution leads to a large energy gap with respect to the negligibly changed (< 0.1 eV) T_{Cz} state, the smaller 0.15-eV reorganisation energy of the partially rotated S_1 in the crystal leads to a 0.26-eV energy gap with respect to T_{Cz} that is comparable to the T_1-S_1 energy gap of 0.17 eV at this geometry. The state labels have been coloured to reflect the emission energy ranges from these states, where observed experimentally. The inset details the results from multireference orbital optimisation for the non-solid-phase (solution) T_1 geometry of CMA1 in isolation.

2.4.3 THE AMORPHOUS PHASE

In between the crystal and solution results is the amorphous-phase emission peak energy that can be thought of as emission from an ensemble of rotamers due to the conformational disorder inherent to kinetic, rather than thermodynamic, control of this phase. Here, we resort to force-field Molecular Dynamics (MD) simulations to sample the conformational space explored by the molecules in a completely amorphous solid, see Methods for details. Room-temperature MD simulations suggest that the molecules can adopt a broad distribution of torsion angles in the ground state, directly reflecting the inhomogeneous environment and lower density of the amorphous phase ($\sim$1.37 g cm^{-3}, compared to 1.53 g cm^{-3} in the crystal, see Experimental Section). As *ab initio* MD simulations in the excited state are prohibitive, we rather performed excited-state geometric relaxation considering the limiting cases of either orthogonal or coplanar orientations. The corresponding lower and upper bounds of the broadened S_1 amorphous-phase emission can then be straightforwardly ascertained by considering spherical clusters of physically reasonable density surrounding a central embedded molecule constrained to that conformation. The simulation results, depicted in **Figure S 7**, indicate that these extrema, computed to be at 2.38 eV for the orthogonal orientation and 2.76 eV for the coplanar orientation, fill the gap between the solution- and crystal-phase emission peak energies. The slightly smaller transition energy (2.76 vs 2.84 eV) obtained for the planar molecule in the amorphous versus crystalline films provides a direct measure for the reduced electrostatic stabilisation associated with the lower density in the amorphous phase. From these simulations, it is apparent that a combination of geometric (conformational) control *and* enhanced polarisation energy in the ordered crystalline phase lead to the most pronounced photoluminescence blueshift. We note that the extent of polarisation-induced S_1-S_0 energetic blueshift determines the viability of S_1-T_{Cz} population transfer, where T_{Cz} is the carbazole-centred LE triplet state, since polarisation pushes the S_1 state closer in energy to the marginally affected locally excited triplet that represents T_2 in the quantum-chemical calculations.

2.4.4 ENERGY LANDSCAPE FOR DIRECT AND REVERSE INTERSYSTEM CROSSING

Nuclear reorganisation in the crystalline singlet excited state (a 21.5° out-of-plane twist) is found to differ negligibly from that in the crystalline/vacuum triplet excited state (19.5° 26.5°) due to torsional restriction. In other words, the potential minimum of S_1 is pushed closer to that of T_1 in the crystalline phase (averting decreased direct S_1-T_1 spin-orbit coupling; see **Table S 3**). As such, the triplet reorganisation energy can be gleaned from an all-QM TDA calculation of the simulated crystal phase at the S_1 optimised geometry. A triplet reorganisation energy for exciton diffusion λ=0.1 eV, taken as half the excitation-energy difference of S_0-T_1 at the ground-state and excited-state geometries, is recovered. This value is in agreement with the experimental result of 0.14 eV and is an anticipated underestimation, given the outstanding nuclear reorganisation in T_1 that is not considered from minimising S_1. It should be mentioned that this reorganisation energy is attributable mostly to intramolecular bond-stretching modes

that are active in all environments. Moreover, when considered alongside the similar activation energies measured for crystal-phase and amorphous-phase emission, this result strongly suggests that complete torsional distortion to achieve the largest reorganisation energy of 0.4 eV (as computed for S_1 at the orthogonal minimum-energy geometry) is not necessary for TADF.

Furthermore, not only is such a large-amplitude change in the torsion angle not required but it is also very much undesired, as the direct spin-orbit coupling (SOC) matrix element $\langle S_1 | H_{SO} | T_1 \rangle$ driving RISC is substantial ($\sim$4 cm^{-1}) at the close-to-planar triplet geometry[31,32], which possesses relatively low symmetry, but decreases by a factor $\sim$20 in the higher symmetry orthogonal configuration[15], in line with theoretical prediction[24,33]. This dramatic reduction in direct S_1-T_1 SOC is fully consistent with El-Sayed's rule and the fact that the states involved should have different spatial wavefunctions for the total (angular plus spin) momentum to be conserved. This turns out to be the case in the sterically constrained solid-state environments but would not be the case for fully twisted molecules. We thus conclude that a partial twist on the triplet potential leads to reverse intersystem crossing without an energetic spin-state inversion, in line with the theoretical prediction by Föller and Marian and Penfold.[9,11].

The T_1 reorganisation energy, computed to be 0.1 eV, not only leads to a narrower energy gap between the relaxed T_1 state of the embedded molecule and neighbouring molecular triplets—thereby facilitating triplet diffusion—but also leads to a narrowed gap between the relaxed S_1 state and the T_{Cz} carbazole triplet on the same embedded molecule. As such, we propose a bifurcation of S_1 population into T_1 and T_{Cz} population at the relaxed crystalline S_1 geometry, as summarised in **Figure 5**. Frustrated nuclear reorganisation and molecular polarisation lead to an S_1 computed emission energy of 2.84 eV—0.17 eV above the T_1 state (2.67 eV) and 0.26 eV below the T_{Cz} state (3.10 eV). As thermally activated delayed fluorescence in the crystal suggests that a $\sim$0.2 eV energy gap can be surmounted, the likely reason for isolated T_{Cz} emission in the crystal is kinetic trapping stemming from constrained coplanarity. At the limit of completely hampered torsional distortion, quantum-chemical calculations suggest that T_{Cz} phosphorescence may appear spectrally "uncovered" below the S_1 emission energy. This T_{Cz} state is a local excitation polarised along the carbazole long axis, leading to a large exchange splitting from the $\sim$305 nm singlet excitation in the solid state (exchange-splitting data can be found in **Table S 3**).

3. CONCLUSIONS

In summary, we developed a method to crystallise CMA1 compounds in-situ using a polar, low glass-transition-temperature matrix and achieved nearly complete crystallisation of the entire thin film. Consequently, we are able to explore the impact of molecular geometry in a controlled manner, contrasting intersystem crossing and emission from constrained coplanar geometries with the behaviour of relaxed rotamers. We find that in the crystalline phase, energetic disorder and the reorganisation energy for triplet diffusion are reduced. Crystallisation also leads to significantly blue-shifted charge-transfer emission. At low temperature, this shift is sufficient to allow observation of structured emission from triplets localised on the carbazole ligand. We explore these

results using QM/MM calculations and find that a combination of restricted torsional relaxation and enhanced electrostatic interactions lead to the modification of the ^{1}CT potential such that a more coplanar conformation is computed to be the equilibrium geometry, resulting in a blueshifted emission peak energy. Because quantum-chemical calculations suggest that the thermal activation energy for CT emission in the absence of spectral migration may be attributed to the exchange energy pushing S_1 above T_1 at a more coplanar triplet geometric optimum, the activation energy is not appreciably altered by material phase—that is, spin crossover does not rely on inter-ligand twisting to orthogonality. Similarly, while photoinduced absorption spectra in crystalline, amorphous and solution phases are distinct, the rate of intersystem crossing appears unaffected by the S_1 equilibrium conformation. We therefore infer that the fairly constant activation energy derived from temperature-dependent photoluminescence spectroscopy reflects the fixed exchange splitting inherent to an unmodified, more coplanar T_1 conformational distribution.

Remarkably, we find that at 300K, emission rates from coplanar crystalline materials are very similar to those observed in the amorphous phase and in isolated, relaxed molecules in solution, despite a 400 meV difference in CT energy. Torsional distortion, in turn, insignificantly impacts the photophysics of TADF organometallics. The real impact comes from an incompletely twisted S_1 distribution of conformers that stabilises T_1, leading to spin-orbit-coupling kinetics that are uniform across CMA1 molecules in different material phases.

4. METHODS

4.1 SYNTHESIS OF CARBENE METAL AMIDES

Carbene metal amides were synthesised as previously reported[2,34,35].

4.2 SAMPLE PREPARATION

Neat amorphous and crystalline thin films (80 wt.% CMA1 in PEO) were made from chlorobenzene solution in 20 mg/mL concentration. These well-mixed solutions were spun inside a nitrogen filled glove box onto pre-cleaned spectrosil substrates at 1,200 r.p.m. for 40 s at room temperature to form thin films. Samples were stored in a nitrogen glovebox to minimise degradation. Solution samples of various solvents were prepared as 1mg/ml in the nitrogen glovebox, deoxygenated and sealed in 1-mm path-length and QS-grade quartz cuvettes.

4.3 UV-VIS-NIR SPECTROPHOTOMETER

A Shimadzu UV-3600 Plus spectrophotometer was used to measure the steady-state absorbance of samples, which comprises three detectors: a PMT (photomultiplier tube) for the ultraviolet and visible regions and InGaAs and cooled PbS detectors for the near-infrared region. The detectable wavelength range is between 185 to 3,300 nm with resolution of 0.1 nm.

4.4 PHOTOLUMINESCENCE SPECTROMETER

An Edinburgh Instruments FLS980 spectrofluorimeter was used to measure steady-state luminescence spectra. A R928P PMT detector was used in this experiment, with a wavelength range of 200 nm to 870 nm and a dark count rate of <50 cps (at -20°C). The detector is operated in single photon counting mode. The PL spectra of CMA1 were collected from 350 nm to 650 nm with the resolution of 1 nm. Samples

were excited by a 450 W Xe1 xenon arc lamp. The light from the xenon arc is focused into the monochromators by using an off-axis ellipsoidal mirror. Absolute photoluminescence quantum efficiency measurements were taken using an integrating sphere under continuous nitrogen purge.

4.5 TEMPERATURE-DEPENDENT NS-MS TIME-RESOLVED PHOTOLUMINESCENCE MEASUREMENTS

Time-resolved photoluminescence spectra were measured by an electrically-gated intensified CCD (ICCD) camera (Andor iStar DH740 CCI-010) connected to a calibrated grating spectrometer (Andor SR303i). Samples were photoexcited by femtosecond laser pulses which were created by second harmonic generation (SHG) in a ß-barium borate crystal from the fundamental source (wavelength = 800 nm, pulse width = 80 fs) of a Ti: Sapphire laser system (Spectra-Physics Solstice), at a repetition rate of 1kHz. The photons from the laser pulses had a wavelength of 400 nm. A 425 nm long-pass filter was used to prevent scattered laser signal from entering the camera. Temporal evolution of the PL emission was recorded by stepping the ICCD gate delay with respect to the trigger pulse. The minimum gate width of the ICCD was 5 ns. Cryogenic measurements were carried out using an Oxford Instruments Optistat continuous flow cryostat with liquid helium coolant, and an ITC 502 S temperature control unit. The 1kHz repetition rate of the laser used in this experiment precludes accurate measure of lifetimes beyond 1 ms.

For non-exponential luminescence decays in the solid state, a characteristic lifetime rather than monoexponential decay time is quoted. We choose the time taken to reach 63% (1-(1/e)) of the total emission integrated from 0 to 950 μs. This allows direct comparison to lifetimes extracted from monoexponential decays.

4.6 MONTE-CARLO SIMULATION PROCEDURE

A cubic lattice with 101x101x101 triplet sites, where site energies were drawn randomly from a Gaussian distribution, was employed for the Monte-Carlo simulation. The initial triplet excitation was placed in the centre of the lattice. The hopping rates to the nearest 125 neighbours were calculated using Eq. (S3). The hopping probability to each site and the overall hopping time were computed with equation Eq. (S4) and Eq. (S5). The triplet excitation was allowed to jump to one of the 125 sites randomly according to the hopping probabilities and the hopping time was added to the total simulation time. The procedures above were repeated until a pre-defined diffusion time was reached. The parameterisation for **Figure 2 b** and **e** is described in detail in the supplementary text.

4.7 TRANSIENT ABSORPTION (TA) SPECTROSCOPY

Solutions of CMA1 and PEO in chlorobenzene were made at 20 mg/ml concentrations, overnight heated at 70 °C to dissolve and mixed in the appropriate ratio (80 wt.% CMA1). Films were drop-cast from solution, 60 μl per film on 13 mm quartz discs heated to 70 °C for neat films and 120 °C for crystalline films. Films were made and kept in a glovebox and encapsulated using a glass slide and epoxy prior to being measured. Drop-cast films had an optical density of 0.4 at 400 nm (the pump wavelength). The pump and probe originate from a Spectra Physics Solstice Ti:Sapphire laser, outputting pulses of width 80 fs and a repetition rate of 1 kHz at 800 nm. The pump beam was frequency-doubled using a BBO to give 400 nm pulses. Excitation fluence was varied from 9-60 μJcm^{-2} using neutral density filters. The probe beam was generated from the 800 nm fundamental using a noncollinear optical parametric amplifier, built in-house. The probe was further split into a probe and reference, with only the probe beam overlapping with the pump on the sample. The pump-probe delay was controlled using a computer-controlled delay stage. A Hamamatsu G11608-512 InGaAs

dual-line array detector was used to measure the transmitted probe and reference.

4.8 X-RAY DIFFRACTION

X-ray diffraction was performed using a Bruker X-ray D8 Advanced diffractometer with Cu K$\alpha_{1,2}$ radiation (λ=1.541 Å). Spectra were collected with an angular range 2θ of 6˚ to 30˚ and Δθ = 0.046˚. Measurement were conducted on drop-cast films.

4.9 RAMAN SPECTROSCOPY

Raman measurements were conducted by back-scattering (HORIBA T64000) a 640 nm (CW diode) line with a subtractive triple-stage. Spectra were collected between 13 and 1770 cm^{-1} where the CCD detector (HORIBA Synapse Open-Electrode) has a monotonically increasing quantum efficiency of between 0.43 and 0.50. Acquisitions employed a 100× optical objective and used minimal laser intensity to avoid laser damage. Drop-cast film samples were measured in air at room-temperature.

4.10 COMPUTATIONAL DETAILS

Gas-phase density functional theory (DFT) calculations of HOMO/LUMO of CMA1 were carried out by the global hybrid MN15 functional by Truhlar and coworkers[36] in combination with the def2-TZVP basis set by Ahlrichs and coworkers.[37,38] Relativistic effective core potential of 60 electrons was used to describe the core electrons of Au.[39] The ground state was studied by DFT and the excited states by time-dependent DFT (TD-DFT).[40] The employed method provides excited state energies that do not suffer from underestimation typical for TD-DFT,[41,42] as indicated by our recent work on closely related molecules[10,43] as well as by comparison to T_1 energies calculated by unrestricted DFT: The unrestricted and TD-DFT T_1 energies differed by only 0.004 eV. These calculations were carried out by Gaussian 16.[44]

TD-DFT calculations under the Tamm-Dancoff Approximation (TDA) were performed using the def2-SVP basis set and a relativistic effective core potential for Au in the context of vertical excitation energies for the various simulated material phases and corresponding geometries. Starting geometric initial guesses were obtained from the CMA1 crystal structure. We used a DFT(PBE1PBE/def2-SVP)-optimised ground-state geometry *in vacuo* for absorption-energy calculations with TDA(PBE1PBE/def2-SVP), taking into account the effect of chlorobenzene solvent using the Polarizable Continuum Model (PCM) state-specific-solvation approach. We used a TDA(PBE1PBE/def2-SVP):UFF hybrid QM:MM (ONIOM) optimised S_1 geometry for crystal emission-energy calculations, with the QM layer consisting only of the molecule being optimised to its S_1 geometry. The embedding molecules were kept frozen in their crystal-structure orientations. In the all-QM calculation of the simulated crystal phase, these frozen orientations, along with the optimised S_1 coordinates of the embedded molecule, were used. The total size of this simulated-crystal-phase supercell was 18 molecules (1602 atoms).

Non-solution excitation energies were computed using all-QM TDA(LC-ω=0.172-PBE/def2-SVP) with the optimally tuned approach in the framework of Koopman's theorem for CMA1. The LC-ω-PBE functional can be used to mitigate self-interaction errors that artificially lower CT excitation energies (an orbital correction) and eliminate the over-stabilising effect of non-exact exchange at particle-hole separation lengths of greater than 1 nm. This approach is most useful for improving the accuracy of intramolecular CT excitation energies as found in CMA1. Improved accuracy is achieved through tuning this range-separated hybrid (RSH) functional that satisfies the asymptotic long-range 1/r distance dependence of electron-hole Coulombic interaction (Hartree-Fock exchange) while nevertheless incorporating DFT exchange for short-range interactions. It is only by turning to such RSH functionals that spurious low-lying intermolecular CT excitations in the all-QM CMA1 cluster can be eliminated, thereby more properly revealing how the lowest-lying intramolecular S_1 CT state is impacted by the CMA1 environment.

For the simulated amorphous phase, spherical supercells of density 1.37 for coplanar and orthogonal embedded molecules—amounting to sizes of 22 and 19 molecules, respectively—were considered for embedded-molecule S_1 optimisation (again freezing the embedding molecules in place). The amorphous phase was constructed by performing molecular mechanics (MM) and molecular dynamics (MD) simulations with the Materials Studio 2018 package using the Universal force field[45] together with atomic charges obtained by fitting the electrostatic potential (ESP charges[46]) calculated at the PBE1PBE/def2-SVP level on an isolated molecule. The procedure used to generate the amorphous phase was the following: (i) 18 molecules were inserted randomly in a large unit cell (50Å * 50Å * 50Å), replicated using periodic boundary conditions to build a 3D infinite system, and subjected to a 500ps MD run at high temperature (NVT, T= 1000K) while keeping the density low (~0.2 g/cm³) to favor a random spatial distribution of the molecules; (ii) 4 successive 500ps-long MD runs (NPT, P = 1atm) were then performed at decreasing temperature (1000K, 750K, 500K, 400K); (iii) finally, a 1ns-long MD simulation (NPT, P = 1 atm, T = 298K) was performed. From the last structure generated during the 1ns-long MD, amorphous spherical clusters containing 22 and 19 molecules (see above) were produced by selecting one random CMA1 and all its neighboring molecules bearing at least one atom within a spherical cutoff of 6Å from any of the atoms of the central CMA1. Note that the Ewald summation method was considered to account for non-bonded interactions in all calculations performed in periodic boundary conditions. As with the crystal-phase computation, geometric optimisation of the central CMA1 molecule of the amorphous spherical clusters was followed by single-point computation with all molecules treated at the QM level using the optimally tuned RSH functional for CMA1.

The solution S_1 geometry was obtained from an initial vacuum-phase S_1 geometric optimisation followed by a solution-phase optimisation in chlorobenzene with the vacuum-phase S_1 optimised geometry as the initial guess. Emission energies in solution were computed from PCM state-specific solvation of S_1 using TDA(PBE1PBE/def2-SVP). For this optimised geometry as well as for the S_1 crystal and S_0 geometries, both singlet and triplet excitation energies up through the T_{Cz} state were considered. For the amorphous phase, however, only the S_1-state excitation energy was considered. Separately, a CMA1 T_1 geometry optimisation was performed *in vacuo* (TDA/PBE1PBE/def2-SVP), followed by a multireference seven-state-averaged four-orbital, four-electron complete-active-space self-consistent-field, or CASSCF(4,4), multireference orbital optimisation with Slater determinants. Valence molecular orbitals optimised at the Hartree-Fock level of theory were utilised as the orbital initial guess for CASSCF(4,4). Spin-orbit coupling was computed between the second and third states from the CASSCF(4,4) output. Each calculation step was carried out using *Gaussian 16*. This procedure was repeated for the optimised S_1 geometry *in vacuo*. All states were identified from the molecular orbitals contributing to their predominant configuration state functions.

ASSOCIATED CONTENT

Supporting Information

Additional photophysical data
Additional computational results
Commentary and details of computational methods
Video of CMA1 crystallization

The Supporting Information is available free of charge on the ACS Publications website.

brief description (file type, i.e., PDF)

brief description (file type, i.e., PDF)

AUTHOR INFORMATION

Corresponding Authors

* Email: dan.credgington@gmail.com (D.C.);
david.beljonne@umons.ac.be (D.B.).

Author Contributions

The manuscript was written through contributions of all authors. All authors have given approval to the final version of the manuscript. †These authors contributed equally.

Notes

Any additional relevant notes should be placed here.

ABBREVIATIONS

CCR2, CC chemokine receptor 2; CCL2, CC chemokine ligand 2; CCR5, CC chemokine receptor 5; TLC, thin layer chromatography.

REFERENCES

[1]   Romanov, A. S., Becker, C. R., James, C. E., Di, D., Credgington, D., Linnolahti, M. & Bochmann, M. Copper and Gold Cyclic (Alkyl)(amino)carbene Complexes with Sub-Microsecond Photoemissions: Structure and Substituent Effects on Redox and Luminescent Properties. *Chem. - A Eur. J.* **23**, 4625–4637 (2017).

[2]   Di, D., Romanov, A. S., Yang, L., Richter, J. M., Rivett, J. P. H., Jones, S., Thomas, T. H., Jalebi, M. A., Friend, R. H., Linnolahti, M., Bochmann, M. & Credgington, D. High-performance light-emitting diodes based on carbene-metal-amides. *Science* **356**, 159–163 (2017).

[3]   Romanov, A. S., Yang, L., Jones, S. T. E., Di, D., Morley, O. J., Drummond, B. H., Reponen, A. P. M., Linnolahti, M., Credgington, D. & Bochmann, M. Dendritic Carbene Metal Carbazole Complexes as Photoemitters for Fully Solution-Processed OLEDs. *Chem. Mater.* **31**, 3613–3623 (2019).

[4]   Romanov, A. S., Jones, S. T. E., Gu, Q., Conaghan, P. J., Drummond, B. H., Feng, J., Chotard, F., Buizza, L., Foley, M., Linnolahti, M., Credgington, D. & Bochmann, M. Carbene metal amide photoemitters: tailoring conformationally flexible amides for full color range emissions including white-emitting OLED. *Chem. Sci.* 7–15 (2019).

[5]   Hamze, R., Shi, S., Kapper, S. C., Ravinson, D. S. M., Estergreen, L., Jung, M. C., Tadle, A. C., Haiges, R., Djurovich, P. I., Peltier, J. L., Jazzar, R., Bertrand, G., Bradforth, S. E. & Thompson, M. E. 'Quick-Silver' from a Systematic Study of Highly Luminescent, Two-Coordinate, d10 Coinage Metal Complexes. *J. Am. Chem. Soc.* **141**, 8616–8626 (2019).

[6]   Hamze, R., Peltier, J. L., Sylvinson, D., Jung, M., Cardenas, J., Haiges, R., Soleilhavoup, M., Jazzar, R., Djurovich, P. I., Bertrand, G. & Thompson, M. E. Eliminating nonradiative decay in Cu(I) emitters: >99% quantum efficiency and microsecond lifetime. *Science* **606**, 601–606 (2019).

[7]   Conaghan, P. J., Menke, S. M., Romanov, A. S., Jones, S. T. E., Pearson, A. J., Evans, E. W., Bochmann, M., Greenham, N. C. & Credgington, D. Efficient Vacuum-Processed Light-Emitting Diodes Based on Carbene–Metal–Amides. *Adv. Mater.* **30**, 1802285 (2018).

[8]   Hall, C. R., Romanov, A. S., Bochmann, M. & Meech, S. R. Ultrafast Structure and Dynamics in the Thermally Activated Delayed Fluorescence of a Carbene-Metal-Amide. *J. Phys. Chem. Lett.* **9**, 5873–5876 (2018).

[9]   Föller, J. & Marian, C. M. Rotationally Assisted Spin-State Inversion in Carbene-Mental-Amides Is an Artifact. *J. Phys. Chem. Lett.* 5643–5647 (2017).

[10]   Romanov, A. S., Jones, S. T. E., Yang, L., Conaghan, P. J., Di, D., Linnolahti, M., Credgington, D. & Bochmann, M. Mononuclear Silver Complexes for Efficient Solution and Vacuum-Processed OLEDs. *Avdanced Opt. Mater.* **6**, 1–5 (2018).

[11]   Thompson, S., Eng, J. & Penfold, T. J. The intersystem crossing of a cyclic (alkyl)(amino) carbene gold (i) complex. *J. Chem. Phys.* **149**, (2018).

[12]   Nobuyasu, R. S., Ward, J. S., Gibson, J., Laidlaw, B. A., Ren, Z., Data, P., Batsanov, A. S., Penfold, T. J., Bryce, M. R. & Dias, F. B. The influence of molecular geometry on the efficiency of thermally activated delayed fluorescence. *J. Mater. Chem. C* **7**, 6672–6684 (2019).

[13]   Dias, F. B., Penfold, T. J. & Monkman, A. Photophysics of thermally activated delayed fluorescence. *Methods Appl. Fluoresc.* 425–463 (2018).

[14]   Dias, F. B., Santos, J., Graves, D. R., Data, P., Nobuyasu, R. S., Fox, M. A., Batsanov, A. S., Palmeira, T., Berberan-Santos, M. N., Bryce, M. R. & Monkman, A. P. The role of local triplet excited states and D-A relative orientation in thermally activated delayed fluorescence: Photophysics and devices. *Adv. Sci.* **3**, 1–10 (2016).

[15]   Taffet, E. J., Olivier, Y., Lam, F., Beljonne, D. & Scholes, G. D. Carbene-Metal-Amide Bond Deformation, Rather Than Ligand Rotation, Drives Delayed Fluorescence. *J. Phys. Chem. Lett.* 1620–1626 (2018).

[16]   Mellerup, S. K. & Wang, S. Boron-Doped Molecules for Optoelectronics. *Trends Chem.* **1**, 77–89 (2019).

[17]   Yamaguchi, N. & Mari, S. Dipole Moment of Poly (ethylene oxide) in Solution and Its Dependence on Molecular Weight and Temperature. *Polym. J.* **41**, 588–594 (2009).

[18]   Faucher, J. A., Koleske, J. V., Santee, E. R., Stratta, J. J. & Wilson, C. W. Glass transitions of ethylene oxide polymers. *J. Appl. Phys.* **37**, 3962–3964 (1966).

[19]   Wang, C., Lili, F., Huazhe, Y., Gongbiao, X., Li, W., Zheng, J., Tian, W. & Li, X. Graphene oxide stabilized polyethylene glycol for heat storage. *Phys. Chem. Chem. Phys.* **14**, 13233–13238 (2012).

[20]   Barron, M. K., Young, T. J., Johnston, K. P. & Iii, R. O. W. Investigation of Processing Parameters of Spray Freezing Into Liquid to Prepare Polyethylene Glycol Polymeric Particles for Drug Delivery. *AAPS PharSciTech* **4**, 1–13 (2003).

[21]   Wang, H., Keum, J. K., Hiltner, A. & Baer, E. Impact of nanoscale confinement on crystal orientation of poly(ethylene oxide). *Macromol. Rapid Commun.* **31**, 356–361 (2010).

[22]   Lai, C. Y., Hiltner, A., Baer, E. & Korley, L. T. J. Deformation of confined poly(ethylene oxide) in multilayer films. *ACS Appl. Mater. Interfaces* **4**, 2218–2227 (2012).

[23]   Rajamalli, P., Senthilkumar, N., Gandeepan, P., Ren-Wu, C. Z., Lin, H. W. & Cheng, C. H. A thermally activated delayed blue fluorescent emitter with reversible externally tunable emission. *J. Mater. Chem. C* **4**, 900–904 (2016).

[24]   Feng, J., Yang, L., Romanov, A. S., Ratanapreechachai, J., Reponen, A.-P. M., Jones, S. T. E., Linnolahti, M., Hele, T. J. H., Köhler, A., Bässler, H., Bochmann, M. & Credgington, D. Environmental Control of Triplet Emission in Donor–Bridge–Acceptor Organometallics. *Adv. Funct. Mater.* **1908715**, 1908715 (2020).

[25]   Gélinas, S., Paré-Labrosse, O., Brosseau, C. N., Albert-Seifried, S., McNeill, C. R., Kirov, K. R., Howard, I. A., Leonelli, R., Friend, R. H. & Silva, C. The binding energy of charge-transfer excitons localized at polymeric semiconductor heterojunctions. *J. Phys. Chem. C* **115**, 7114–7119 (2011).

[26]   Rao, A., Chow, P. C. Y., Gélinas, S., Schlenker, C. W., Li, C. Z., Yip, H. L., Jen, A. K. Y., Ginger, D. S. & Friend, R. H. The role of spin in the kinetic control of recombination in organic photovoltaics. *Nature* **500**, 435–439 (2013).

[27]   Movaghar, B., Grünewald, M., Ries, B., Bässler, H. & Würtz, D. Diffusion and relaxation of energy in disordered organic and inorganic materials. *Physical Review B* **33**, 5545–5554 (1986).

[28]   Tamm, I. Relativistic Interaction of Elementary Particles. *J. Phys.(USSR)* **9**, 449 (1945).

[29]   Hirata, S. & Head-Gordon, M. Time-dependent density functional theory within the Tamm-Dancoff approximation. *Chem. Phys. Lett.* **314**, 291–299 (1999).

[30]   S.M. Dancoff. Non-Adiabatic Meson Theory of Nuclear Forces. *Phys. Rev.* **78**, 382–385 (1950).

[31]   Marian, C. M. Spin-orbit coupling and intersystem crossing in molecules. *Wiley Interdiscip. Rev. Comput. Mol. Sci.* **2**, 187–203 (2012).

[32]   Plotnikov, V. G. Regularities of the processes of radiationless conversion in polyatomic molecules. *Int. J. Quantum Chem.* **16**, 527–541 (1979).

[33]   Hele, T. J. H. & Credgington, D. Theoretical description of Carbene-Metal-Amides. Physics.chem-ph. 1802 (2018). *arxiv:*1802.00804

[34]   Conaghan, P. J., Matthews, C. S. B., Chotard, F., Jones, S. T. E., Greenham, N. C., Bochmann, M., Credgington, D. & Alexander S. Romanov. Highly Efficient Blue Host-Free and Host-Guest Organic Light-Emitting Diodes Based on Carbene-Metal-Amides. *Nat. Comm.* 11(1):1758 (2020).

[35]   Feng, J., Yang, L., Romanov, A. S., Ratanapreechachai, J., Jones, S. T. E., Reponen, A.-P. M., Linnolahti, M., Hele, T. J. H., Köhler, A., Bässler, H., Bochmann, M. & Credgington, D. Environmental Control of Triplet Emission in Donor-Bridge-Acceptor Organometallics. *Adv. Funct. Mater.* **1908715**, (2020).

[36]   Yu, H. S., He, X., Li, S. L. & Truhlar, D. G. MN15: A Kohn-Sham global-hybrid exchange-correlation density functional with broad accuracy for multi-reference and single-reference systems and noncovalent interactions. *Chem. Sci.* **7**, 5032–5051 (2016).

[37]   Weigend, F. & Ahlrichs, R. Balanced basis sets of split valence, triple zeta valence and quadruple zeta valence quality for H to Rn: Design and assessment of accuracy. *Phys. Chem. Chem. Phys.* **7**, 3297–3305 (2005).

[38]   Weigend, F., Häser, M., Patzelt, H. & Ahlrichs, R. RI-MP2: optimized auxiliary basis sets and demonstration of efficiency. *Chem. Phys. Lett.* **294**, 143–152 (1998).

[39]   Andrae, D., Häußermann, U., Dolg, M., Stoll, H. & Preuß, H. Energy-adjusted *ab initio* pseudopotentials for the second and third row transition elements. *Theor. Chim. Acta* **77**, 123–141 (1990).

[40]   Furche, F., Rappoport, D. & Olivuccim, M. *Density functional methods for excited states: equilibrium structure and electronic spectra in Computational Photochemistry.* (Elesvier, Amsterdam, 2005).

[41]   Dreuw, A. & Head-Gordon, M. Single-Reference ab Initio Methods for the Calculation of Excited States of Large Molecules. *Chem. Rev.* **105**, 4009–4037 (2005).

[42]   Moore, B., Sun, H., Govind, N., Kowalski, K. & Autschbach, J. Charge-Transfer Versus Charge-Transfer-Like Excitations Revisited. *J. Chem. Theory Comput.* **11**, 3305–3320 (2015).

[43]   Romanov, A. S., Yang, L., Jones, S. T. E., Di, D., Morley, O. J., Drummond, B. H., Reponen, A. P. M., Linnolahti, M., Credgington, D. & Bochmann, M. Dendritic Carbene Metal Carbazole Complexes as Photoemitters for Fully Solution-Processed OLEDs. *Chem. Mater.* **31**, 3613–3623 (2019).

[44]   Frisch, M. J., Trucks, G. W., Schlegel, H. B., Scuseria, G. E., Robb, M. A. & R., C. J. Gaussian 16, Revision A. 03. Gaussian. Inc., Wallingford CT (2016).

[45]   Rappé, A. K., Casewit, C. J., Colwell, K. S., Goddard, W. A. & Skiff, W. M. UFF, a Full Periodic Table Force Field for Molecular Mechanics and Molecular Dynamics Simulations. *J. Am. Chem. Soc.* **114**, 10024–10035 (1992).

[46]   Besler, B. H., Merz, K. M. & Kollman, P. A. Atomic charges derived from semiempirical methods. *J. Comput. Chem.* **11**, 431–439 (1990).

1
2
3
4
5
6
7
8
9
10
11
12
13
14
15
16
17
18
19
20
21
22
23
24
25
26
27
28
29
30
31
32
33
34
35
36
37
38
39
40
41
42
43
44
45
46
47
48
49
50
51
52
53
54
55
56
57
58
59
60

1
2
3
4
5
6
7
8
9
10
11
12
13
14
15
16
17
18
19
20
21
22
23
24
25
26
27
28
29
30
31
32
33
34
35
36
37
38
39
40
41
42
43
44
45
46
47
48
49
50
51
52
53
54
55
56
57
58
59
60

^{3}LE

S_1

T_1

ISC

Crystallization